Chemistry–A European Journal
Research Article
doi.org/10.1002/chem.202201358
Chemistry Europe
European Chemical Societies Publishing
www.chemeurj.org

Acene Size-Dependent Transition of The Radical Centers From the Metal to The Acene Parts In Monocationic Dinuclear (Diethynylacene)diyl Complexes

Yuya Tanaka,*[a, b] Reo Kawano,[b] and Munetaka Akita*[a, b]

Abstract: Controlling radical localization/delocalization is important for functional materials. The present paper describes synthesis and results of electrochemical, spectroscopic, and theoretical studies of diruthenium (*p*-diethynylacene)diyl complexes, Me_3Si-$(C{\equiv}C)_2$-Ru(dppe)$_2$-C≡C–Ar-C≡C–Ru(dppe)$_2$-$(C{\equiv}C)_2$-$SiMe_3$ (**1**–**6**) (dppe: 1,2-bis(diphenylphosphino)ethane), and their monocationic radical species ([**1**]$^+$–[**6**]$^+$). The HOMO-LUMO energy gaps can be finely tuned by the acene rings in the bridging ligands installed, as indicated by the absorption maxima of the electronic spectra of **1**–**6** ranging from the UV region even to the NIR region. The cationic species [**1**]$^+$–[**6**]$^+$ show two characteristic NIR bands, which are ascribed to the charge resonance (CR) and π-π* transition bands, as revealed by spectroelectrochemistry. Expansion of the acene rings in [**1**]$^+$–[**6**]$^+$ causes (1) blue shifts of the CR bands and red shifts of the π-π* transition bands and (2) charge localization on the acene parts as evidenced by the ESR, DFT and TD-DFT analyses. Notably, the monocationic complexes of the larger acene derivatives are characterized as the non-classical acene-localized radicals.

Introduction

Electron transfer (ET) from a donor to an accepter is a ubiquitous phenomenon, which frequently occurs in biological systems and molecular materials. To obtain fundamental understanding of the inter- and intra-molecular ET processes, numerous model systems have been developed. In this regard, the dinuclear mixed-valence (MV) complex [L_nM-BL-ML_n]$^{+\bullet}$ (M: metal, L_n: ligands, BL: bridging ligand) is an excellent model for the intramolecular ET processes repeatedly occurring between the two metal centers (Figure 1a).[1–8] The metal fragment and the bridging ligand largely affect the radical distribution. MV complexes with the oxidized metal centers and those with the oxidized ligands are called metal-localized and ligand-localized states, respectively. In reality, however, the charge is more or less delocalized over the whole [L_nM-BL-ML_n]$^{+\bullet}$ structure. Thus, in this paper, we classified the charged states into further four categories depending on the degree of metal oxidation (Figure 1b). When the radical is mainly localized on the metal centers but partially delocalized over the BL, we call it *metal-delocalized state*. When the radical is mainly delocalized over the BL with the partially oxidized metal center, we call it *ligand-delocalized state*. These states have been frequently called "metal-centered" and "ligand/bridge-centered" states, respectively, in the literature.[3,5,8] When the majority of radicals are localized on the metal fragments or the ligands, such situations are regarded as *metal-localized* and *ligand-localized states*, respectively. MV complexes are also categorized according to the Robin-Day classification, i.e. on the basis of equal (class III) or unequal charge distribution (class II) on the two metal centers. Because the properties of the MV complexes are dependent on the extent of distribution of the radical cation over the molecules, exploration of the effects of combinations of the metal fragments and the bridging ligands is essential to understand and control the physical properties of the MV complexes.

Neutral dinuclear bridging acetylide complexes having electron-rich metal fragments L_nM–C≡C–R–C≡C–ML_n (R; none, alkynediyl, arylene) can be converted to the monocationic MV complexes upon 1e-oxidation. Due to the variable π-bonding interactions between the metal d and ligand p orbitals, charge-delocalization characters of the MV complexes drastically vary depending on the metal fragments and R used.[3,5,8] For example, in the case of the MV complexes with the (butadiyne)diyl linker [Cp*M(dppe)-$(C{\equiv}C)_2$-Cp*M(dppe)]$^{+\bullet}$ (Cp*: 1,2,3,4,5-pentamethylcyclopentadienyl; M: Fe, Ru; dppe: 1,2-bis(diphenylphosphino)ethane), the iron complex tends to

[a] *Dr. Y. Tanaka, Prof. Dr. M. Akita*
Laboratory for Chemistry and Life Science
Institute of Innovative Research
Tokyo Institute of Technology
4259 Nagatsuta, Midori-ku, Yokohama 226-8503 (Japan)
E-mail: ytanaka@res.titech.ac.jp

[b] *Dr. Y. Tanaka, R. Kawano, Prof. Dr. M. Akita*
Department of Chemical Science and Engineering
School of Materials and Chemical Technology
Tokyo Institute of Technology
4259 Nagatsuta, Midori-ku, Yokohama 226-8503 (Japan)
E-mail: ytanaka@res.titech.ac.jp
akitatit@icloud.com

Supporting information for this article is available on the WWW under https://doi.org/10.1002/chem.202201358

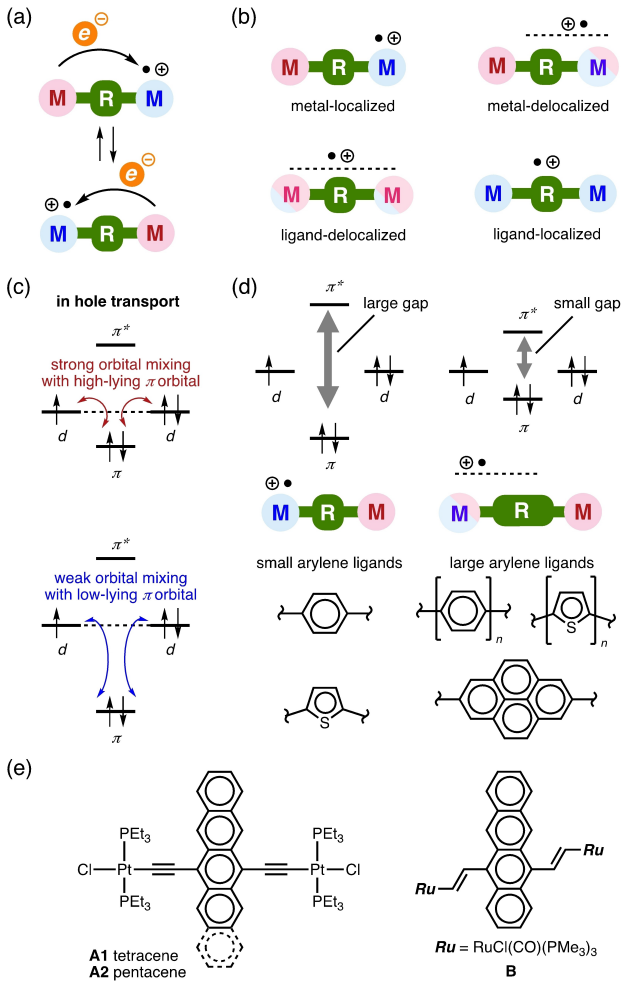

Figure 1. (a) Metal-to-metal electron transfer (ET) processes of MV complexes and (b) classification of mono-oxidized states of dinuclear complexes in this manuscript. (c) Orbital diagrams of MV complexes with high- and low-lying π-orbitals (d) MV complexes with single and extended arylene ligands. (e) Examples of metal complexes with extended diethynyl- and divinyl-acene ligands.

show the metal-localized state, whereas the ruthenium complex prefers the ligand-delocalized state.[9]

Control of the energy levels of the BLs is a key to tune the charge-localization/delocalization. Effective charge delocalization over the BL is promoted by, for a hole, raising the π orbital energy level of the BL to enhance the orbital mixing with the metal d orbitals (Figure 1c).[2] One approach to achieve effective charge delocalization is to decrease the HOMO-LUMO gap of the BLs (Figure 1d). Therefore, numerous reports on metal alkynyl MV complexes with extended aromatic π-conjugated systems (R = arylene) have appeared to date as exemplified by those with the oligophenylene,[10] oligothiophene,[11] pyrene[12] and porphyrin moieties.[13–15] (Diethynylacene)diyls are fascinating candidates for the BLs because extension of the acene size causes narrowing of the HOMO-LUMO gaps of the BL parts, which should bring about the stronger π interactions to lead to the charge delocalization over the molecule. In contrast to the many MV complexes of dinuclear (diethynylacene)diyl complexes with smaller acene rings such as benzene, naphthalene, and anthracene,[16–20] the larger tetracene and pentacene derivatives have scarcely been reported,[21] while metal-higher acene conjugates have been an interest for theoretical studies.[22–24] Yip et al. described the synthesis and photophysical properties of the diplatinum complexes with the (5,12-diethynyltetracene)diyl (**A1**) and (6,13-diethynylpentacene)diyl BLs (**A2**),[25–27] but no redox chemistry has been unveiled due to the poor redox activity of the platinum fragments (Figure 1e). As a related work, Liu reported the diruthenium complex **B** with the 5,12-divinyltetracene linker (Figure 1e).[28] Unfortunately, because the tetracene complex underwent irreversible redox processes, the corresponding MV complex could not be studied in detail.

Herein, we report the synthesis and charge-delocalization properties of the dinuclear metal acetylide-type complexes **1**–**6** bearing the various (*p*-diethynylacene)diyl linkers (Figure 2) and the electron-rich $Ru(dppe)_2$ fragments.[29–36] The diethynylacene linkers studied here involve diethynyl-benzene (**1**), -naphthalene (**2**), -anthracene (**3**, **4**), -tetracene (**5**) and -pentacene derivatives (**6**). The systematic study revealed that the location of the radical centers in the MV species was dependent on the acene moieties, varying from the conventional metal-delocalized and ligand-delocalized states to the non-classical ligand-localized states (Figure 1b).[37]

Results and Discussion

Synthesis and characterization

The dinuclear complexes **1**–**6** were prepared by treatment of $Ru(dppe)_2Cl(C_4TMS)$ with the corresponding diethynylacenes in 15–44% yields following the method previously established for the $Ru(dppe)_2$-acetylide complexes.[36,38,39] The C_4TMS moieties improved solubility in common organic solvents and will allow further functionalization towards application as molecular wires.[34,36] For the anthracene complexes, two isomeric derivatives **3** (1,4-substituted) and **4** (9,10-substituted) were prepared. Attention should be paid to handling of the terminal acetylene precursors for the tetracene and pentacene complexes, because they formed insoluble films upon concentration due to oligomerization (see the experimental section). The dinuclear

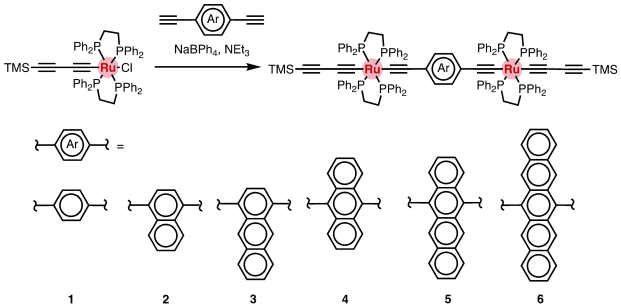

Figure 2. Synthetic scheme and molecular structures of the dinuclear (diethynylacene)diyl ruthenium complexes **1**–**6**.

complexes **1**–**6** were stable in solutions under a nitrogen atmosphere, and in the solid-state under ambient conditions. Their $^{31}P\{^{1}H\}$ NMR spectra show single singlet signals ascribed to the dppe ligands, indicating highly symmetrical structures with the *trans* arrangements of the acetylide ligands. Multiple ν(C≡C) vibrational frequencies are well characterized by the IR spectroscopy, and the lowest energy vibrational frequencies shift to the lower energies as the acene rings are expanded (**1**: 1995 cm^{-1}, **2**: 1996 cm^{-1}, **3**: 1997 cm^{-1}, **4**: 1942 cm^{-1}, **5**: 1935 cm^{-1}, **6**: 1928 cm^{-1}). These shifts should be due to the increased π-back donation from the metal centers to the diethynylacene ligands caused by the lowering of the LUMO levels of the acene parts. The solid-state structures of **1**–**6** are shown in Figure 3.[40] Contrary to the IR results, the C≡C bond lengths do not reveal strong correlation with the ring sizes of the acene moieties (1.19–1.26 nm). Similarly, the Ru–Ru spatial distances are virtually the same (1.22–1.24 nm). These results suggest that the ring sizes of the acene moieties do not affect the solid-state structures of the neutral complexes significantly. While organic acene compounds often reveal π-π stacking interactions in their crystals owing to their large π-surface areas, the acene moieties in **1**–**6** are isolated from each other in the crystal lattices due to the bulky $Ru(dppe)_2$ groups, which prevent intermolecular interactions between the acene moieties.

Electrochemistry

We performed electrochemical measurements of **1**–**6** ([complexes] = ~1.0 mM in CH_2Cl_2, $[NBu_4][PF_6]$ = 0.1 M, W.E. and C.E.: Pt, R.E.: Ag/Ag^+) and the results are summarized in Table 1 and Figure 4. Two fully reversible, well-separated 1e-oxidation waves were observed within the solvent window, which revealed the substantial interaction between the two Ru centers. As the aromatic rings are expanded, the first oxidation waves ($E^1_{1/2}$ vs. $FeCp_2/FeCp_2^+$) shift to the low potential side from −180 (for **1**) to −620 mV (for **6**) in accord with the ascending HOMO levels. The potential separations between the two waves (ΔE) increase from **1** (310 mV) to **2** (320 mV) and then to **4** (365 mV), while those for **5** (355 mV) and **6** (360 mV) are virtually the same as that of **4**. The ΔE value of **3** (1,4-substituted isomer; 305 mV) is smaller than that of **4** (9,10-substituted isomer) but comparable to those of **1** and **2**. It should be noted that, in addition to the metal-metal interaction, many factors such as solvation, ion-pairing, electrostatic repulsion, and magnetic interactions affect the ΔE values.[5,41] Thus, quantitative analysis based on the comproportionation constants K_C needs attention. Nevertheless, the large K_C values (10^5 to 10^6) suggest the strong metal-metal interactions between the two ruthenium centers in **1**–**6**, and their 1e-oxidized MV species are expected to be stable and populated enough to be observed under the electrochemical conditions.

UV-vis-NIR absorption spectra

UV-vis-NIR absorption spectra of **1**–**6** revealed the characteristic features of the acene moieties (Figure 5a). The lowest energy bands' maxima gradually shift from the UV (369 nm for **1**) to NIR region (785 nm for **6**) as the acene ring sizes are expanded. Furthermore, the vibrational structures are observed for the

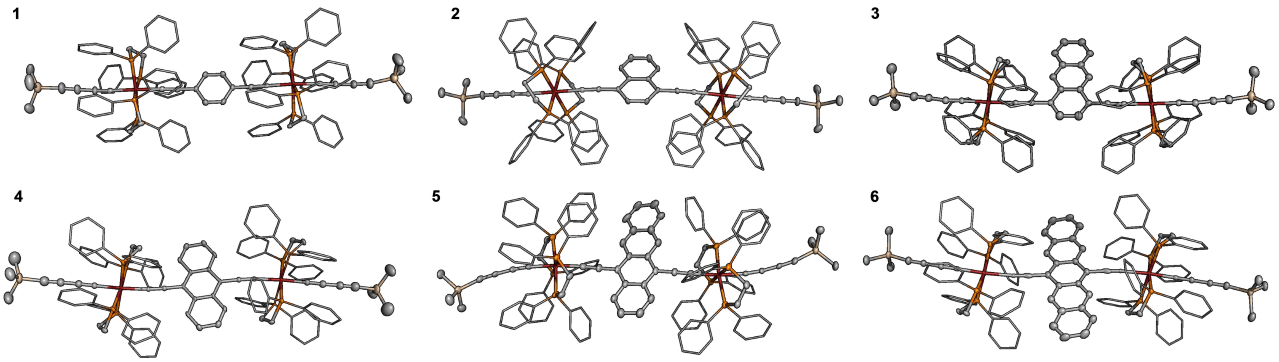

Figure 3. X-ray structures of **1**–**6**. Thermal ellipsoids are set at the 50% probability levels. Hydrogen atoms and solvent molecules are omitted for clarity. Phenyl rings in the dppe ligands are drawn with wire models.

Table 1. CV data for **1**–**6**.[a]

	E^1_{pa} [mV]	E^1_{pc} [−]	ΔE^{1} [b]	$E^1_{1/2}$	E^2_{pa}	E^2_{pc}	ΔE^{2} [b]	$E^2_{1/2}$	ΔE [c]	K_C [d]	
1	−139	−221	82	−180	171	89	82	130	310	1.8×10^5
2	−223	−309	86	−266	97	10	86	54	320	2.6×10^5
3	−273	−359	86	−316	27	−49	75	−11	305	1.5×10^5
4	−366	−463	97	−415	4	−103	107	−50	365	1.5×10^6
5	−516	−580	64	−548	−156	−230	74	−193	355	1.0×10^6
6	−570	−670	100	−620	−210	−310	100	−260	360	1.2×10^6

[a] [complexes] = ~1.0 mM in CH_2Cl_2, $[NBu_4][PF_6]$ = 0.1 M, W.E. and C.E.: Pt, R.E.: Ag/Ag^+. [b] $\Delta E^n = E^n_{pa} - E^n_{pc}$. [c] $\Delta E = E^2_{1/2} - E^1_{1/2}$. [d] $K_C = \exp(F/RT \times \Delta E)$.

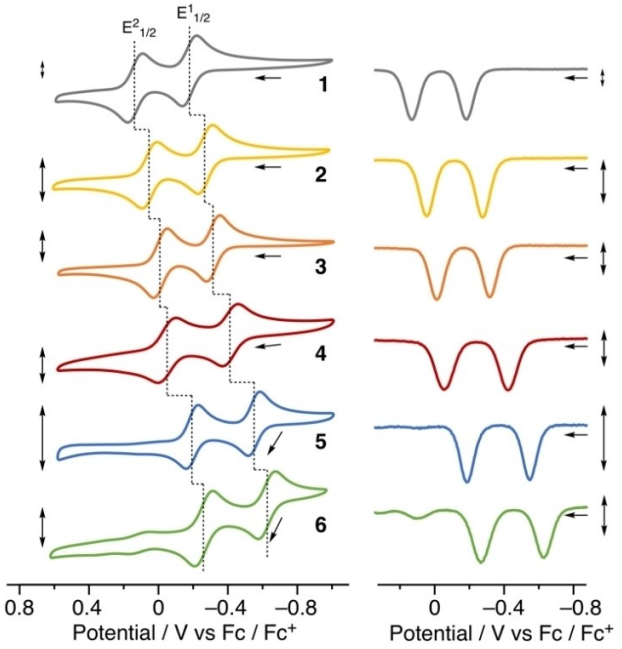

Figure 4. CV and DPV charts for **1**–**6** ([complexes] = ~1.0 mM in CH_2Cl_2, $[NBu_4][PF_6]$ = 0.1 M, W.E. Ag mesh, C.E.: Pt, and R.E.: Ag/Ag^+.). Scale bars for current are 2 μA (CV) and 10 μA (DPV), respectively. Scan rates were set to 100 mV/s (CV) and 20 mV/s (DPV).

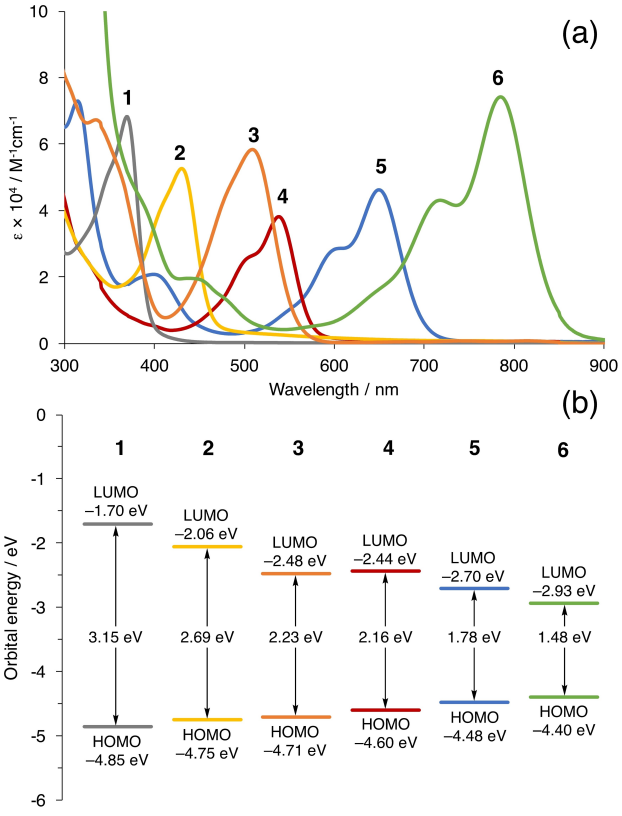

Figure 5. (a) UV-vis-NIR absorption spectra of **1**–**6** (in CH_2Cl_2). (b) HOMO-LUMO energy diagrams of **1**–**6** estimated by the CV and UV-vis-NIR absorption studies. For the estimation method of HOMOs and LUMOs energies, see Supporting Information.

lowest-energy bands. The frontier orbital energy diagrams estimated from the CV and UV-vis-NIR absorption studies are shown in Figure 5b. The HOMO energy levels are raised (from −4.85 (**1**) to −4.40 eV (**6**)) with the expansion of the acene ring sizes, while the LUMO energy levels are lowered (from −1.70 (**1**) to −2.93 eV (**6**)). The energy difference of the LUMOs ($\Delta_{6\text{-}1}$ = 1.23 eV) is larger than that of the HOMOs ($\Delta_{6\text{-}1}$ = 0.45 eV). These results demonstrate that the frontier orbital energies are finely tunable by the acene moieties.

To get insight into the frontier orbital characters, we carried out DFT calculations for **1′**-**6′**, where the terminal TMS groups of **1**–**6** were replaced with the hydrogen atoms (Figure 6). The electron-rich, larger acene moieties (with the higher HOMOs) increase their contributions to the HOMOs from **1′** (21%) to **6′** (59%). The LUMOs bear the predominant contribution of the π* orbitals of the acene moieties for **3′**-**6′** (>80%), while the contributions of the Ru d orbitals and the p orbitals of the dppe ligands are prominent for **1′**. Thus, the expansion of the acene moieties causes the rise of the HOMO levels and lowering of the LUMO levels to significantly diminish the HOMO-LUMO gaps, reflecting the character of the original acenes.

Spectroelectrochemistry

Spectroscopic features of 1e-oxidized species of the dinuclear complexes provide us with essential information on the charge localization/delocalization phenomena. Spectroelectrochemical measurements of **1**–**6** were carried out under the same conditions as those of the electrochemical ones (Figure 7a and Table 2, [complexes] = ~1.0 mM in CH_2Cl_2, $[NBu_4][PF_6]$ = 0.1 M, W.E.: Ag mesh, C.E.: Pt, R.E.: Ag/Ag^+.). Upon oxidation of **1**–**6** under applied bias voltages, the strong NIR absorption bands ascribed to the MV species $[\mathbf{1}]^+$–$[\mathbf{6}]^+$ appeared. Further oxidation under higher bias voltages led to the disappearance of the NIR bands and the appearance of the new bands around 600–1200 nm, suggesting occurrence of a second oxidation process. While the observed NIR bands for $[\mathbf{1}]^{+\cdot}$–$[\mathbf{6}]^+$ are characteristic of the dinuclear species with the substantial metal-metal interactions, the new bands ascribed to the dicationic species are featureless regardless of the BLs except $[\mathbf{1}]^{2+}$.

Charge-delocalization properties of the MV species $[\mathbf{1}]^+$–$[\mathbf{6}]^+$ can be discussed on the basis of the NIR absorption bands. Two types of the absorption bands are observed in the vis-NIR region. The broad bands have been ascribed to charge resonance (CR) bands rather than intervalence charge transfer (IVCT) bands. This is because the character of the transition changes depending on the BLs, and the charges are delocalized over the entire molecules, and therefore the redox site becomes not obvious (see below).[42,43] The other bands associated with the vibronic structures are characterized as the π-π* transitions of the acene moieties. The vibrational spacings are ca. 1450 cm^{-1}, which is typical for aromatic C–C stretching vibrations.

The NIR bands for $[\mathbf{1}]^+$–$[\mathbf{6}]^+$ are deconvoluted into the three Gaussian curves (A–C, Figure 7b and Table 3). For $[\mathbf{5}]^+$ and $[\mathbf{6}]^+$,

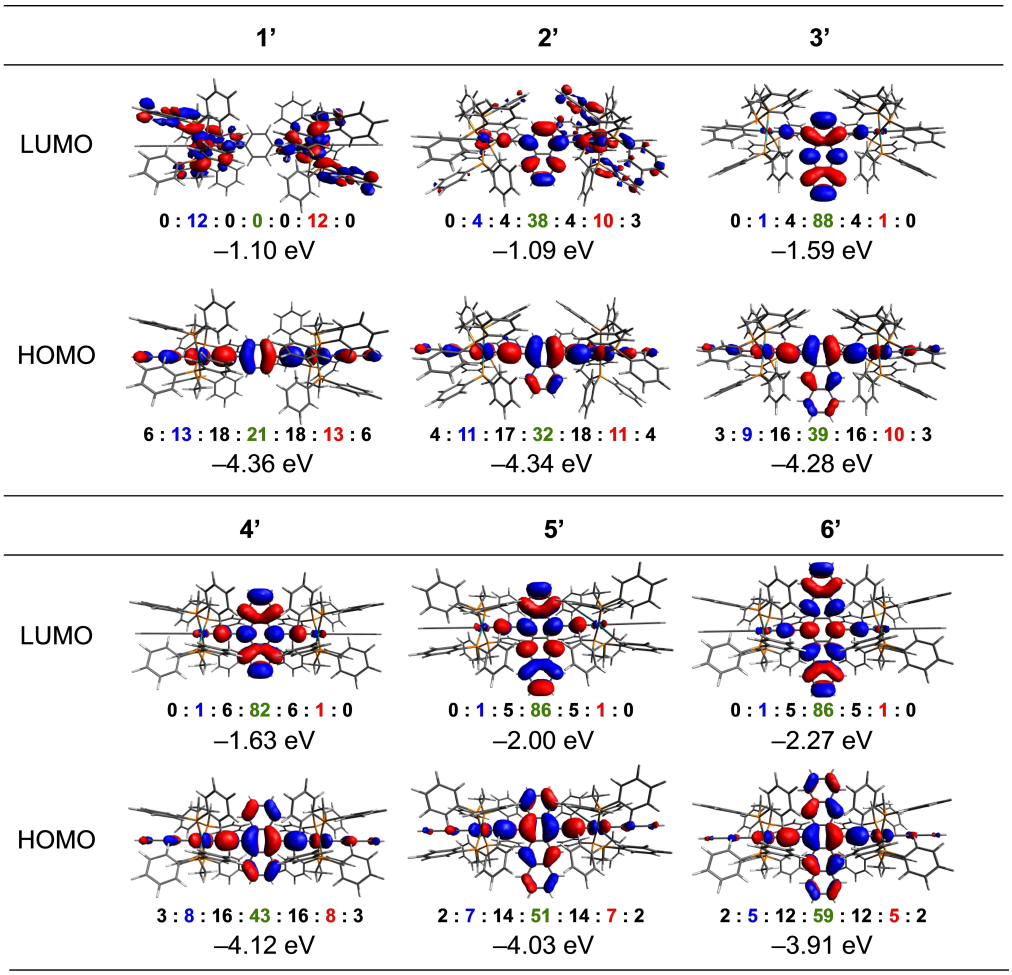

Figure 6. Frontier orbitals, their energies, and contributions of the H–C≡C, Ru, C≡C, and acene moieties of **1'-6'**. DFT calculations were performed at the B3LYP/LanL2DZ (Ru), 6-31G(d) (C, H, P), CPCM (CH_2Cl_2) level of theory.

Table 2. UV-vis-NIR absorption spectral data for $[1]^{n+}$–$[6]^{n+}$ ($n=0$–2).[a]

complex	λ_{max}/nm ($\varepsilon\times10^{-4}$/$M^{-1}cm^{-1}$) $n=0$	$n=1$	$n=2$
$[1]^{n+}$	369 (18.10)	1797 (10.57), 501 (7.81)	608 (10.28)
$[2]^{n+}$	430 (5.26)	1609 (5.97), 659 (4.18), 590 (3.72)	1066 (8.51)
$[3]^{n+}$	509 (5.83)	1525 (5.96), 816 (4.07), 742 (3.48)	1037 (11.19)
$[4]^{n+}$	538 (3.82)	1316 (2.91), 899 (3.31), 804 (2.73)	938 (3.75)
$[5]^{n+}$	650 (4.63)	1177 (4.35), 1010 (3.81)	910 (3.75)
$[6]^{n+}$	718 (4.30), 785 (7.41)	589 (3.03), 1107 (5.93), 1609 (6.13)	560 (4.96), 916 (9.41)

[a] in CH_2Cl_2, $[NBu_4][PF_6]=0.1$ M, W.E. and C.E. Pt, R.E. Ag/Ag^+.

Table 3. Deconvoluted vis-NIR absorptions data for $[1]^{n+}$–$[6]^{n+}$ ($n=0$–2) .

	Band	ν_{max}/cm^{-1}	ε_{max}/$M^{-1}cm^{-1}$	$\nu_{1/2}$/cm^{-1}		Band	ν_{max}/cm^{-1}	ε_{max}/$M^{-1}cm^{-1}$	$\nu_{1/2}$/cm^{-1}
$[1]^+$	A	5551	96096	1370	$[4]^+$	A	7550	28233	1430
	B	7000	46809	2250		B	9150	8972	1560
	C	10500	22520	5000					
$[2]^+$	A	6135	52710	1201	$[5]^+$	A	8470	18457	2075
	B	7650	16862	1800		B	9100	6554	1800
	C	9200	8608	6100		C	12000	10639	3000
$[3]^+$	A	6500	58140	1430	$[6]^+$	A	8850	47374	1600
	B	8160	16224	1500		B	10430	28034	1480
	C	9750	13759	2250		C	12440	13771	1970

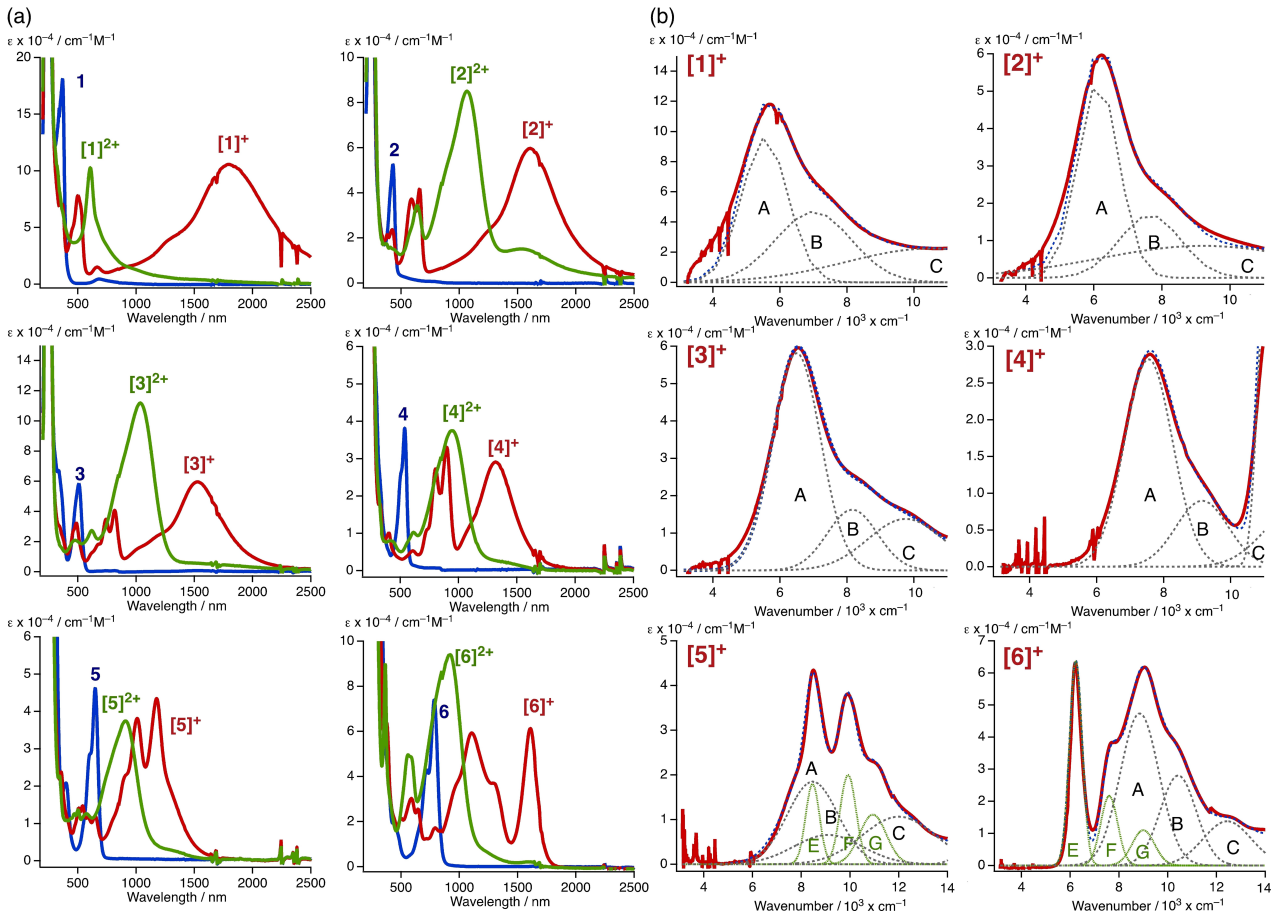

Figure 7. (a) Vis-NIR absorption spectra of $[\mathbf{1}]^{n+}$–$[\mathbf{6}]^{n+}$ (n = 0–2) upon applied bias voltages (in CH_2Cl_2, $[NBu_4][PF_6]$ = 0.1 M, W.E. and C.E.: Pt, R.E.: Ag/Ag^+, neutral: blue, monocation: red, dication: green.) (b) Deconvolution analyses of the NIR bands for $[\mathbf{1}]^+$–$[\mathbf{6}]^+$. The gray dashed (CR bands) and green dotted lines (π-π* bands) are deconvoluted curves.

the additional three curves (D–F) are required to reproduce the π-π* transition of the acene moieties.[2] The recent computational studies by Kaupp revealed that the multiple NIR bands originated from thermodynamically accessible rotamers.[44] Besides, the bands, in addition to the IVCT character, bear MLCT (metal to ligand charge transfer), LMCT (ligand to metal charge transfer), and LLCT (ligand to ligand charge transfer) characters, and their contributions are variable depending on the electronic structures. The lowest energy bands of the deconvoluted CR bands (band A) shift to the higher energies in accord with the expansion of the ring sizes ($[\mathbf{1}]^+$: 5551→$[\mathbf{2}]^+$: 6135→$[\mathbf{3}]^+$: 6500→$[\mathbf{4}]^+$: 7550→$[\mathbf{5}]^+$: 8470→$[\mathbf{6}]^+$: 8850 cm^{-1}), whereas the trend is opposite for the π-π* transitions ($[\mathbf{1}]^+$: 19960→$[\mathbf{2}]^+$: 15175→$[\mathbf{3}]^+$: 12255→$[\mathbf{4}]^+$: 11123→$[\mathbf{5}]^+$: 8465→$[\mathbf{6}]^+$: 6230 cm^{-1}). Good correlations between the HOMO energies estimated by CV and the absorption maxima ν_{max} of bands A and π-π* transitions are noted (Figure 8). These trends indicate that not only the π-π* transitions but also bands A (the most intense CR bands) are dominated by the electronic effects of the acene moieties.

To gain further insight into the NIR transition bands, we carried out TD-DFT study of $[\mathbf{1'}]^+$–$[\mathbf{6'}]^+$ at the UBLYP35-D3/

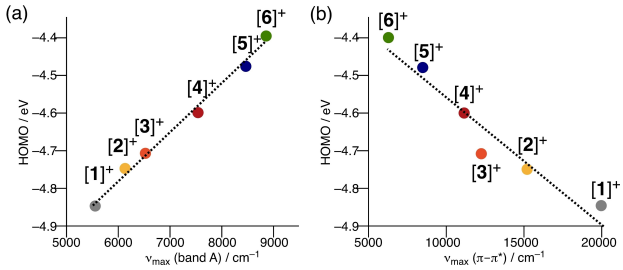

Figure 8. Plots of HOMO levels against (a) ν_{max} of band A and (b) ν_{max} of π-π* transition bands.

Def2SVP(CPCM;CH_2Cl_2) levels of theory.[44,45] The NIR absorption band energies are well consistent with bands A and π-π* transition bands (Figure 9, Table 4). Although the calculated CR band energy is lower than the experimental energy for the pentacene derivative $[\mathbf{6'}]^+$, the theoretical result is qualitatively coincident with the acene size-dependent shifts of the CR and π-π* transition bands mentioned above. Of the π-π* transition bands, the α-HOSO-to-α-LUSO transitions play the dominant roles with the exception of $[\mathbf{1'}]^+$, which undergoes the dominant α-HOSO-to-α-LUSO+1 transition derived from CT

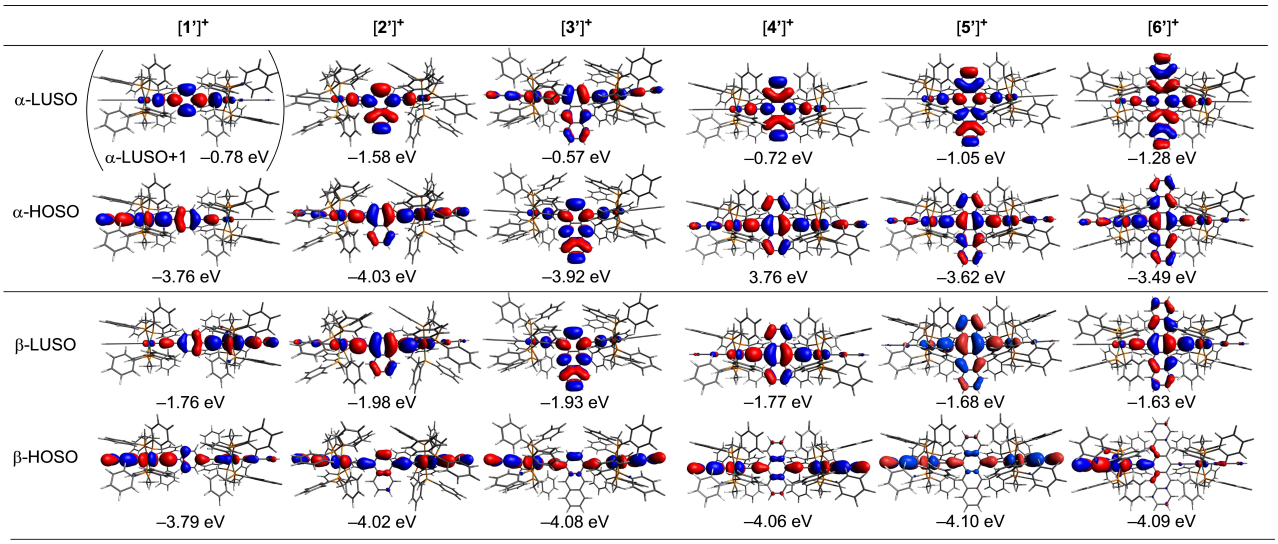

Figure 9. The HOSO and LUSO for $[\mathbf{1'}]^+$–$[\mathbf{6'}]^+$.

Table 4. Assignments of vis-NIR absorptions for $[\mathbf{1'}]^+$–$[\mathbf{6'}]^+$.

	$\nu_{max}^{exp.}$/cm^{-1}	$\nu_{max}^{DFT[b]}$/cm^{-1} (nm)	oscillator strength	main transition	assignment
$[\mathbf{1}]^+/[\mathbf{1'}]^+$	5551 (1801)[a]	7968 (1255)	0.7320	β-HOSO→β-LUSO (74%)	IVCT
	19960 (501)	18051 (554)	0.1265	α-HOSO→α-LUSO+1 (21%)	ML/LLCT
$[\mathbf{2}]^+/[\mathbf{2'}]^+$	6235 (1604)[a]	6079 (1645)	0.9597	β-HOSO→β-LUSO (92%)	ML/LLCT
	15175 (659)	15552 (643)	0.3197	α-HOSO→α-LUSO (61%)	π-π* transition
$[\mathbf{3}]^+/[\mathbf{3'}]^+$	6500 (1538)[a]	6911 (1447)	0.9400	β-HOSO→β-LUSO (80%)	ML/LLCT
	12255 (816)	15898 (629)	0.2241	α-HOSO→α-LUSO (30%)	π-π* transition
$[\mathbf{4}]^+/[\mathbf{4'}]^+$	7550 (1325)[a]	8410 (1189)	0.9841	β-HOSO→β-LUSO (77%)	ML/LLCT
	11123 (899)	10929 (915)	0.1268	α-HOSO→α-LUSO (75%)	π-π* transition
$[\mathbf{5}]^+/[\mathbf{5'}]^+$	8470 (1180)[a]	10050 (995)	0.2131	β-HOSO→β-LUSO (63%)	ML/LLCT
	8465 (1177)[a]	6378 (1568)	0.4876	α-HOSO→α-LUSO (61%)	π-π* transition
$[\mathbf{6}]^+/[\mathbf{6'}]^+$	8850 (1130)[a]	14341 (697)	0.3013	β-HOSO→β-LUSO (15%)	ML/LLCT
	6230 (1609)[a]	4847 (2063)	0.3406	α-HOSO→α-LUSO (74%)	π-π* transition

[a] Obtained by the deconvolution analysis. [b] Calculated by the UBLYP35-D3/Def2SVP(CPCM;CH_2Cl_2) levels of theory.

from the Ru-C_4H moiety to the diethynylbenzene moiety (Figure 9). On the other hand, contributions of the π-π* transitions of the acene moieties increase with expansion of the acene ring sizes.

The broad absorption bands for $[\mathbf{1'}]^+$ originate from the β-HOSO-to-β-LUSO transitions, which bear the IVCT character with some contribution of the diethynylbenzene ligand (Figure 9). On the other hand, the larger acene complexes $[\mathbf{2'}]^+$–$[\mathbf{5'}]^+$ undergo transitions from the C_4-Ru–C≡C–Ar-C≡C–Ru-C_4 parts with the quinoid resonance structure (C=C=Ar=C=C) to the Ru–C≡C–Ar-C≡C–Ru parts. The feature likely results from the bridge-delocalized class III character. Interestingly, the pentacene derivative $[\mathbf{6'}]^+$ shows an absorption due to the ML/LLCT transition from the Ru-C_4H moiety to the diethynylpentacene moiety. In this case, the β-HOSO is localized on one side of the molecule. Although the CR transitions change from IVCT to ML/LLCT with the expansion of the sizes of the acene rings, the good correlation between the HOMO energies and ν_{max} of the CR bands A is shown as noted above (Figure 8). This suggests that the balance of the redox potentials between the ruthenium centers and the acene moieties determines the transition characters of the CR bands. Because the CR bands contain a significant degree of the diethynylacene character, estimation of the electronic coupling based on the two-state Marcus-Hush theory is not appropriate. On the other hand, the subtle solvent-dependence of the NIR transitions (in acetone vs. in CH_2Cl_2; $\Delta\nu_{max} < 200$ cm^{-1}, Figure S8) suggests that the NIR transitions of the MV complexes $[\mathbf{1'}]^+$–$[\mathbf{6'}]^+$ bear little CT character caused by the changes of the dipole moments of the molecules. If the monocationic species $[\mathbf{1'}]^+$–$[\mathbf{6'}]^+$ are categorized into the classical metal-localized MV complexes, they are classified into the strongly coupled class II or class III systems according to the Robin and Day classification.[46]

ESR study

To investigate the character of the MV radical species, we carried out electron spin resonance (ESR) measurements of $[\mathbf{1}]^+$–$[\mathbf{6}]^+$. Metal-localized *d* radicals and ligand-localized π radicals

can be distinguished on the basis of the features of the *g*-tensors, i.e. rhombic (*d* radical) or isotropic *g*-tensor (π radical). The ESR signals of open-shell organometallic complexes often reveal mixed *d*-π radical characters and, thus, the observed *g*-tensors exhibit both of the *d* and π radical features. To quantitatively analyze the *g*-tensor, discussion has been made on the basis of the following two values. One is anisotropic factor Δg ($=g_1$-g_3); the larger the *d* radical character, the larger the Δg value. The other is isotropic value g_{iso} ($=(g_1+g_2+g_3)/3$). When π radical character increases, the g_{iso} value approaches 2.0023 (the value for free organic radicals). The MV species $[\mathbf{1}]^+$–$[\mathbf{6}]^+$ were generated in situ by addition of 0.9 equiv. of $[FeCp_2][PF_6]$ to CH_2Cl_2 solutions of **1**–**6** at room temperature, and the ESR spectra were recorded at both room temperature and 78 K (Figure 10, Table 5). The ESR spectrum of $[\mathbf{1}]^+$ contains a rhombic signal when observed at 78 K, indicating the radical is mainly localized on the metal centers. As the acene ring sizes in the BLs are expanded, the anisotropic factors decrease (Δg, 0.152 for $[\mathbf{1}]^+$ to ~0 for $[\mathbf{6}]^+$) and the isotropic values approach 2.0023 (g_{iso}, 2.062 for $[\mathbf{1}]^+$ to 2.016 for $[\mathbf{6}]^+$). These results suggest that the larger acene derivatives bear the more π radical character. On the other hand, the broad signal for $[\mathbf{1}]^+$ observed at room temperature indicates the increased metal-based radical character, whereas the sharp isotropic signal with the narrow band width observed for $[\mathbf{6}]^+$ suggests the radical center residing on the diethynylacene moiety. The *g*-tensor for the pentacene derivative $[\mathbf{6}]^+$ without hyperfine coupling is in sharp contrast to those with the hyperfine couplings of the monocations generated from the unsubstituted[47] and 6,13-bis(triisopropylsilylethynyl)-substituted pentacenes.[48] Although the ligand-localized oxidation states have been reported for the MV complexes with diruthenium divinylarene linkers,[49] only a few examples can be found for the diruthenium (diethynylarene)diyl systems.

Table 5. ESR data obtained at 78 K and room temperature (in parentheses) in CH_2Cl_2.

Complex	g_1	g_2	g_3	g_{iso}[a]	Δg[b]
$[\mathbf{1}]^+$	2.146	2.045	1.994	2.062(2.055)	0.152
$[\mathbf{2}]^+$	2.097	2.043	2.041	2.047(2.047)	0.095
$[\mathbf{3}]^+$	2.080	2.041	2.000	2.040(2.039)	0.080
$[\mathbf{4}]^+$	2.058	2.026	1.999	2.028(2.029)	0.059
$[\mathbf{5}]^+$	2.046	2.024	2.001	2.024(2.022)	0.045
$[\mathbf{6}]^+$	–[c]	–[c]	–[c]	2.016(2.017)	–[c]

[a] $g_{iso}=(g_1+g_2+g_3)/3$, [b] $\Delta g=g_1-g_3$.[c] An isotropic signal was observed.

Spin density of the MV complexes

Spin density plots obtained by the DFT calculations nicely support the ESR results as compared with the mononuclear counterparts $[\mathbf{7'}]^+$–$[\mathbf{12'}]^+$ (Figure 11). The spin densities of the benzene derivative $[\mathbf{1'}]^+$ are localized on the C_4-Ru-C_2-C_6H_4-C_2 part to leave the other Ru-C_4 moiety non-oxidized, while those of the derivatives with the larger acene rings $[\mathbf{2'}]^+$–$[\mathbf{6'}]^+$ mainly localize on the diethynylacene moieties. The spin densities on the Ru atoms decrease monotonously, as the acene size is expanded ($[\mathbf{1'}]^+$: 78→$[\mathbf{2'}]^+$: 31→$[\mathbf{3'}]^+$: 25/$[\mathbf{4'}]^+$: 20→$[\mathbf{5'}]^+$: 14→$[\mathbf{6'}]^+$: 12). Based on the spin densities, these MV complexes are categorized into metal-delocalized ($[\mathbf{1'}]^+$), ligand-delocalized ($[\mathbf{2'}]^+$- $[\mathbf{4'}]^+$), and ligand(acene)-localized states ($[\mathbf{5'}]^+$ and $[\mathbf{6'}]^+$) (Figure 1b) On the other hand, for the mononuclear counterparts, the changes of the spin densities on the Ru atoms are rather moderate ($[\mathbf{7'}]^+$: 96→$[\mathbf{8'}]^+$: 95→$[\mathbf{9'}]^+$: 90/$[\mathbf{10'}]^+$: 80→$[\mathbf{11'}]^+$: 70→$[\mathbf{12'}]^+$: 64) and the spin densities are spread

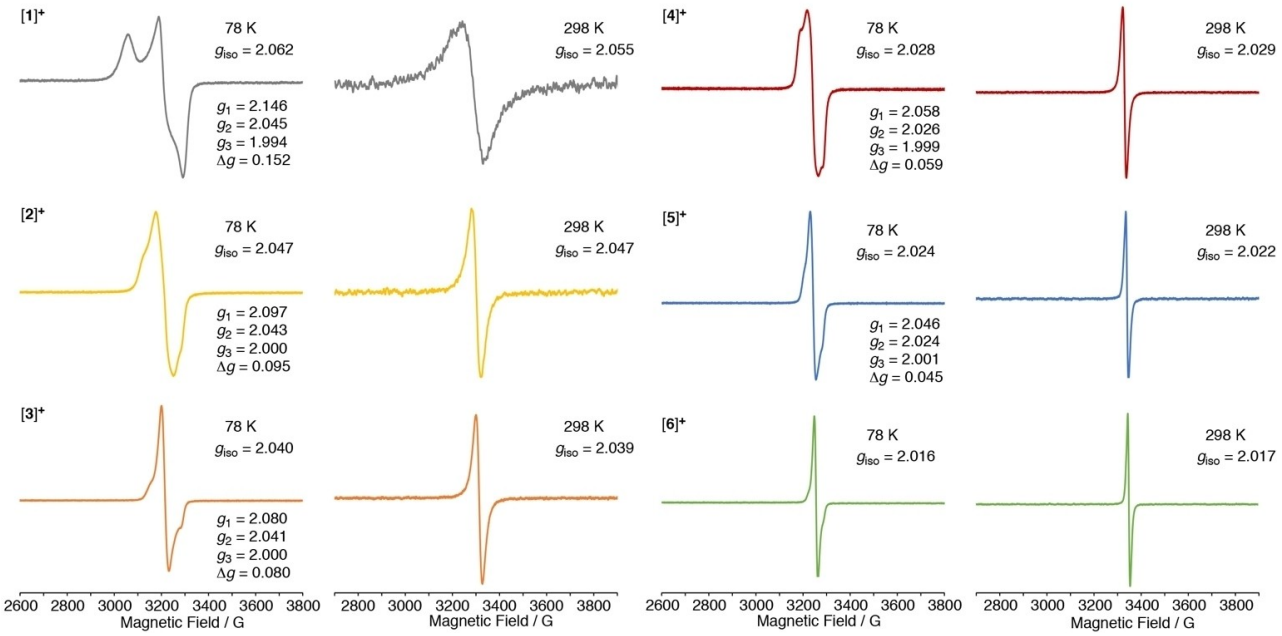

Figure 10. ESR spectra for $[\mathbf{1}]^+$–$[\mathbf{6}]^+$ (left; CH_2Cl_2 glasses observed at 78 K, right; CH_2Cl_2 solutions observed at room temperature).

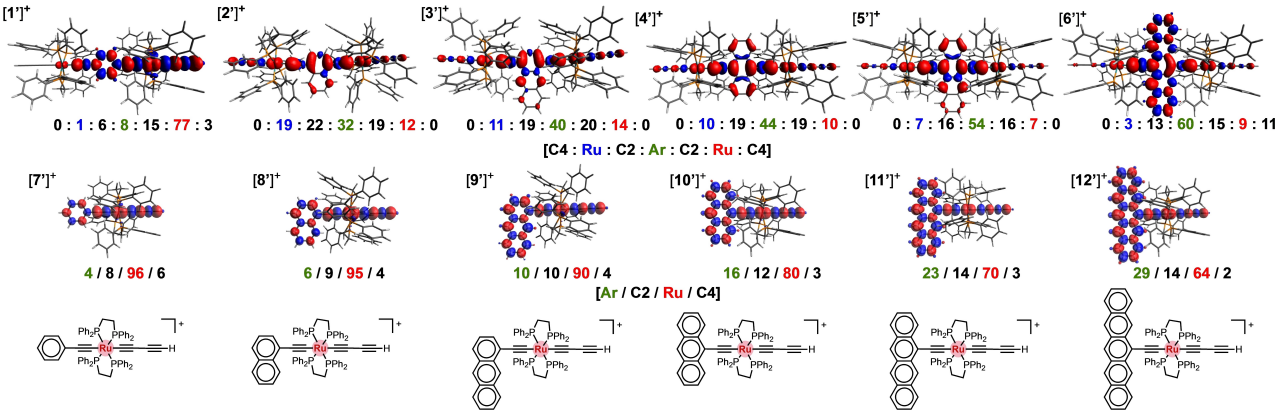

Figure 11. Spin density plots of $[1']^+$–$[12']^+$ and molecular structures of $[7']^+$–$[12']^+$. The α- and β-spin distributions are represented in red and blue, respectively.

over the whole molecules. Consequently, the expansion of the $d\pi$-$p\pi$ systems by the attachment of the terminal HC_4RuC_2 fragment induces the charge localization on the diethynylacene moieties.

Discussion on the charge localization/delocalization

As described above, MV complexes $[\mathbf{1}]^+$–$[\mathbf{6}]^+$ turn out to show a variety of features depending on the location of the radical centers, i.e. the metal-delocalized, ligand-delocalized, and ligand(acene)-localized charged states. To discuss these MV states on the basis of energy potential diagrams, we have to consider the three-state models.[50] For simplicity, however, we here discuss the qualitative analysis. The parabolic energy potentials (G_M) constitute a potential surface with the double minima for weakly coupled two-state systems (Figure 12a). Assuming that the metal-metal coupling V_{MM} is constant regardless of the BLs, the adiabatic potential surfaces are affected by the metal-bridging ligand coupling V_{ML} and the potential differences between G_M and the BL's potential (G_{BL}) (Figure 12b).

For 3D model, the BL's surface placed arbitrarily along the symmetric reaction coordinate from the metal-localized states. For the benzene derivative $[\mathbf{1}]^+$, the G_{BL} should contribute but the large energy gap between G_M and G_{BL} makes the contribution of G_{BL} small (Figure 13). As the ring size is expanded, the G_{BL} surface is shifted to the lower energy and contributes to the adiabatic potential surface. At some point, the adiabatic potential forms a single minimum, leading to the class III species with the substantial contribution of the ligand-localized radical. Expansion of the acene rings causes lowering of the energies of the BL's surface and further localization of the radical on the acene parts as can be seen for the pentacene derivative $[\mathbf{6}]^+$. Thus, extension of the central aromatic π-systems leads to the smooth transition from the metal-localized class II state to the ligand-delocalized class III species and then to the non-classical ligand-localized states.

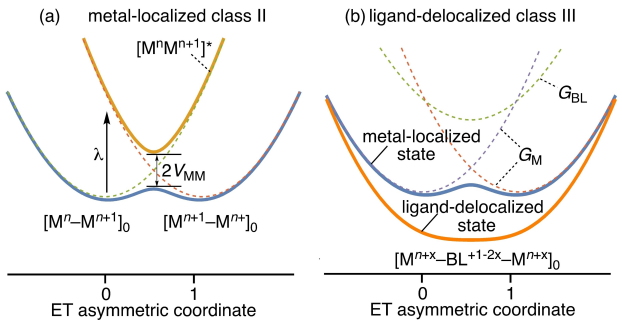

Figure 12. 2D potential diagrams of diabatic (dashed-lines) and adiabatic potential curves (solid-lines) for (a) metal-localized class II and (b) ligand-delocalized class III states. G_M and G_{BL} represent potential curves for the metal-localized and ligand-localized species, respectively. The adiabatic potential curve of the ligand-delocalized state and G_{BL} are placed along the symmetric coordinate, which is perpendicular to the asymmetric coordinate.

Conclusion

The present study reports on synthesis and physicochemical properties of the neutral and 1e-oxidized monocationic MV species of the diruthenium complexes with the diethynylacene-diyl bridges (**1**–**6** and $[\mathbf{1}]^+$–$[\mathbf{6}]^+$) including the rare examples of the tetracene (**5**) and pentacene derivatives (**6**). The electronic structures of $[\mathbf{1}]^{n+}$–$[\mathbf{6}]^{n+}$ ($n = 0$, 1) reflect the characters of the acene rings in the BLs as revealed by the electrochemical and spectroscopic studies. As the acene BL sizes are expanded, the charges in the cationic species $[\mathbf{1}]^+$–$[\mathbf{6}]^+$ tend to localize on the acene moieties as evidenced by the ESR study. The good correlation between the HOMO levels and the energies of the deconvoluted NIR bands observed for the MV species reveals that radical characters are strongly dependent on the balance of the orbital energies between the Ru fragments and the diethynylacenes in the BLs. Notably, in the pentacene derivative $\mathbf{6}^+$, the charge is localized on the pentacene moiety. Expansion of the central acene rings leads to the smooth transition from

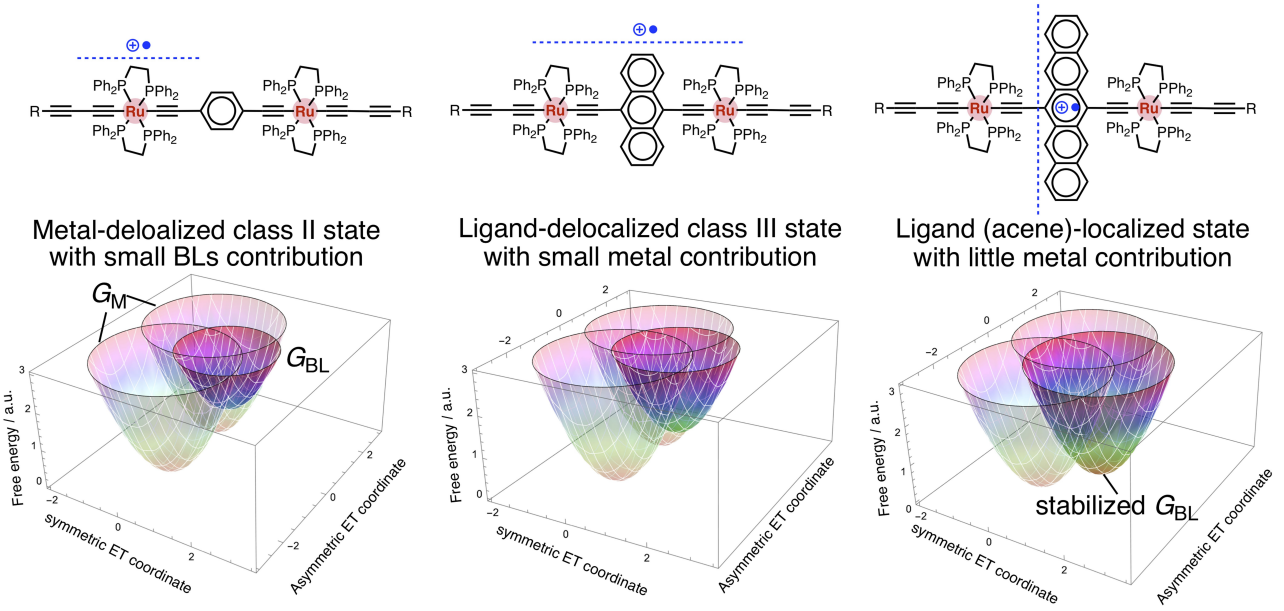

Figure 13. Schematic representations of charge delocalization for the monocationic diethynylacene complexes and the corresponding 3D potential diagrams of diabatic potential parabolae for the metal-localized (G_M, translucent) and ligand-localized (G_{BL}, solid) oxidized species.

the metal-delocalized class II state to the ligand-delocalized class III states and then to the non-classical ligand-localized oxidation states. The modification of the acene-containing bridging ligands enables the fine tuning of the frontier orbital energies and charge localization/delocalization properties, providing platforms suitable to molecular wires. Single-molecule conductance study of the related complexes are currently ongoing in our laboratory.[34,36,51,52]

Experimental Section

General procedure for the preparation of diethynylacene precursors

Method A (for 2–4): To a mixture of bis(trimethylsilylethynyl)acene (0.1–0.6 mmol scale) and KOH (4 equiv.) was added THF (3–5 mL) and MeOH (2–3 mL), and the mixture was stirred for 2 h at room temperature. The reaction mixture was evaporated *in vacuo* and the residue was extracted with CH_2Cl_2 and passed through a short silica gel pad. The filtrate was evaporated to afford the diethynylacene.

Method B (for 5 and 6): A suspension of bis(trimethylsilylethynyl)acene (0.02–0.05 mmol scale) and KOH (pellets, 10 equiv.) in toluene (10–20 mL) and EtOH or MeOH (2–4 mL) was sonicated with ultrasound for 20 min, and stirred for 2 h at room temperature. The reaction mixture was concentrated (~10 mL) *in vacuo*, and the obtained solution was passed through a short silica gel pad (eluted with CH_2Cl_2 for diethynyltetracene and with toluene for diethynylpentacene) to afford a solution of the desilylated diethynylacenes. For the tetracene derivative, the volatiles were evaporated and used immediately for the next step without further purification. On the other hand, for the pentacene derivative, its solution could be stored for a short period but must not be evaporated completely because it causes film caused by the polymerization.

Synthesis of the ruthenium complexes 1–6

Synthesis of 1: To a mixture of $RuCl(C_4TMS)(dppe)_2$ (60 mg, 0.057 mmol), $NaBPh_4$ (24 mg, 0.071 mmol) and triethylamine (0.5 mL) dissolved in 1,2-dichloroethane (2 mL) was added 1,4-diethynylbenzene (3.0 mg, 0.024 mmol) and the resultant mixture was stirred for 1 day at room temperature. The volatiles were evaporated *in vacuo* and the residue was purified by aluminum oxide column chromatography (CH_2Cl_2/hexane = 1:1) to afford a yellow powder of **1** (23 mg, 0.010 mmol, 44%). The product is pure enough for various measurements. An analytical pure sample and crystals for X-ray analysis were obtained by slow diffusion of MeOH into a CH_2Cl_2 solution of **1**. ^{1}H NMR (400 MHz, $CDCl_3$, r.t.): δ 0.22 (s, 18H, TMS), 2.51–2.75 (m, 16H, dppe-CH_2), 6.68 (s, 4H, C_6H_4), 7.00 (t, J = 7.6 Hz, 16H, *m*-C_6H_5), 7.04 (t, J = 7.6 Hz, 16H, *m*-C_6H_5), 7.09–7.16 (m, 16H, *o*-C_6H_5), 7.19 (t, J = 7.6 Hz, 8H, *p*-C_6H_5), 7.25 (t, J = 7.6 Hz, 8H, *p*-C_6H_5), 7.73–7.84 (m, 16H, *o*-C_6H_5). ^{31}P{^{1}H} NMR (161 MHz, $CDCl_3$, r.t.): δ 53.1 (s, dppe). ^{13}C{^{1}H} NMR (126 MHz, CD_2Cl_2): δ 1.20 (s, TMS), 31.8 (t, J = 12.2 Hz, dppe-CH_2), 68.2 (s, $C{\equiv}C$), 95.8 (s, $C{\equiv}C$), 99.3 (s, $C{\equiv}C$), 118.5 (s, *ipso*-C_6H_4), 126.0 (s, $C{\equiv}C$), 127.5 (s, *m*-C_6H_5), 128.4 (quint, J = 15.5 Hz, Ru$\equiv C$), 129.1 (s, *p*-C_6H_5), 129.3 (s, *p*-C_6H_5), 129.6 (s, C_6H_4), 134.3 (s, *o*-C_6H_5), 134.9 (quint, J = 15.1 Hz, Ru$\equiv C$), 134.9 (s, *o*-C_6H_5), 136.6 (quint, J = 10.2 Hz, *ipso*-C_6H_5), 137.4 (quint, J = 10.2 Hz, *ipso*-C_6H_5). ESI-TOF MS (CH_2Cl_2): *m/z* Calcd. for $C_{128}H_{118}P_8Ru_2Si_2$: 2162.48, Found 2162.35 $[M]^+$. IR (KBr/cm^{-1}): 1995 (m), 2069 (s), 2111 (s), 2167 (m) ν(C≡C). Anal. Calcd. for $C_{128.3}H_{118.6}Cl_{0.6}P_8Ru_2Si_2$ (**1**·$(CH_2Cl_2)_{0.3}$): C, 70.43; H, 5.46, Found: C, 70.36; H, 5.54.

In the following synthesis, analytical pure samples and crystals for X-ray analysis were obtained by recrystallization by slow diffusion of hexane into CH_2Cl_2 solutions of the diruthenium complexes, unless otherwise stated.

Synthesis of 2: The title complex **2** was prepared in a manner similar to that of **1** using $RuCl(C_4TMS)(dppe)_2$ (138 mg, 0.131 mmol), $NaBPh_4$ (58 mg, 0.170 mmol), triethylamine (1.0 mL), 1,2-dichloroethane (8 mL), and 1,4-diethynylnaphtalene (10 mg, 0.057 mmol, prepared by using the method A) as a yellow powder (19 mg, 0.009 mmol, 15%). ^{1}H NMR (400 MHz, $CDCl_3$, r.t.): δ 0.22 (m, 18H,

TMS), 2.53–2.82 (m, 16H, dppe-CH_2), 6.66 (s, 2H, $C_{10}H_6$), 6.88–6.99 (m, 16H, *m*-C_6H_5), 6.88–6.99 (m, 16H, *o*-C_6H_5), 6.99–7.07 (m, 2H, $C_{10}H_6$), 6.99–7.07 (m, 16H, *o*-C_6H_5), 7.13–7.23 (m, 16H, *p*-C_6H_5), 7.66–7.88 (m, 2H, $C_{10}H_6$), 7.95–8.14 (m, 16H, *o*-C_6H_5). $^{31}P\{^1H\}$ NMR (161 MHz, $CDCl_3$, r.t.): δ 53.7 (s, dppe). ESI-TOF MS (CH_2Cl_2): *m/z* Calcd. for $C_{132}H_{120}P_8Ru_2Si_2$: 2212.50, Found 2212.37$[M]^+$. IR (KBr/cm^{-1}): 1996 (m), 2052 (s), 2112 (s), 2169 (m) ν(C≡C). Anal. Calcd. for $C_{132.3}H_{120.6}Cl_{0.6}P_8Ru_2Si_2$ (**2**·$(CH_2Cl_2)_{0.3}$): C, 71.00; H, 5.43, Found: C, 70.99; H, 5.88.

Synthesis of 3: The title complex **3** was prepared in a manner similar to that of **1** using RuCl(C_4TMS)$(dppe)_2$ (50 mg, 0.047 mmol), $NaBPh_4$ (22 mg, 0.064 mmol), triethylamine (0.5 mL), 1,2-dichloroethane (8 mL), and 1,4-diethynylanthracene (5.0 mg, 0.022 mmol, prepared by using the method A) as a orange powder of **3** (17 mg, 0.008 mmol, 36%). ^1H NMR (400 MHz, C_6D_6, r.t.): δ 0.24 (s, 18H, TMS), 2.53–2.80 (m, 16H, dppe-CH_2), 6.83–6.93 (m, 16H, *m*-C_6H_5), 6.83–6.93 (m, 8H, *p*-C_6H_5), 6.83–6.93 (s, 2H, $C_{14}H_8$), 7.02 (m, *J* = 7.2 Hz, 16H, *m*-C_6H_5), 7.07 (m, *J* = 7.2 Hz, 8H, *p*-C_6H_5), 7.13–7.24 (m, 2H, $C_{14}H_8$), 7.25–7.32 (m, 16H, *o*-C_6H_5), 7.48–7.53 (m, 2H, $C_{14}H_8$), 8.04–8.14 (m, 16H, *o*-C_6H_5), 8.73 (s, 2H, $C_{14}H_8$). $^{31}P\{^1H\}$ NMR (162 MHz, C_6D_6, r.t.): δ 53.2 (s, dppe). ESI-TOF MS (CH_2Cl_2): *m/z* Calcd. for $C_{136}H_{122}P_8Ru_2Si_2$: 2262.51, Found 2262.10 $[M]^+$. IR (KBr/cm^{-1}): 1997 (m), 2049 (s), 2113 (s), 2168 (m) ν(C≡C). Anal. Calcd. for $C_{136}H_{122}P_8Ru_2Si_2$ (**3**): C, 72.20; H, 5.44, Found: C, 71.84; H, 5.46.

Synthesis of 4: The title complex **4** was prepared in a manner similar to that of **1** using RuCl(C_4TMS)$(dppe)_2$ (53 mg, 0.050 mmol), $NaBPh_4$ (22 mg, 0.064 mmol), triethylamine (0.5 mL), 1,2-dichloroethane (3 mL), and 9,10-diethynylanthracene (5.0 mg, 0.021 mmol, prepared by using the method A) as a red powder of **4** (10 mg, 0.004 mmol, 22%). ^1H NMR (400 MHz, C_6D_6, r.t.): δ 0.43 (s, 18H, TMS), 2.63–2.82 (m, 16H, dppe-CH_2), 6.76 (t, *J* = 7.2 Hz, 16H, *m*-C_6H_5), 6.87 (t, *J* = 7.2 Hz, 8H, *p*-C_6H_5), 6.91–6.95 (m, 4H, $C_{14}H_8$), 7.01 (t, *J* = 7.2 Hz, 16H, *m*-C_6H_5), 7.06 (t, *J* = 7.2 Hz, 8H, *p*-C_6H_5), 7.22–7.30 (m, 16H, *o*-C_6H_5), 8.00–8.13 (m, 16H, *o*-C_6H_5), 8.21–8.30 (m, 4H, $C_{14}H_8$). $^{31}P\{^1H\}$ NMR (161 MHz, C_6D_6, r.t.): δ 51.4 (s, dppe). ESI-TOF MS (CH_2Cl_2): *m/z* Calcd. for $C_{136}H_{122}P_8Ru_2Si_2$: 2262.51, Found 2262.26 $[M]^+$. IR (KBr/cm^{-1}): 1942 (m), 2010 (s), 2113 (s), 2169 (m) ν(C≡C). Anal. Calcd. for $C_{136}H_{122}P_8Ru_2Si_2$ (**4**): C, 72.20; H, 5.44, Found: C, 72.13; H, 5.41.

Synthesis of 5: The title complex **5** was prepared in a manner similar to that of **1** using RuCl(C_4TMS)$(dppe)_2$ (70 mg, 0.068 mmol), $NaBPh_4$ (32 mg, 0.092 mmol), triethylamine (0.5 mL), 1,2-dichloroethane (8 mL), and 5,12-diethynyltetracene (8.0 mg, 0.030 mmol, freshly prepared by using the method B) as a blue powder of **5** (21 mg, 0.0094 mmol, 30%). An analytical pure sample and crystals for X-ray analysis were obtained by slow diffusion of hexane into a benzene solution of **5**. ^1H NMR (400 MHz, C_6D_6, r.t.): δ 0.44 (s, 18H, TMS), 2.71–2.86 (m, 16H, dppe-CH_2), 6.69 (t, *J* = 7.2 Hz, 16H, *m*-C_6H_5), 6.76 (t, *J* = 7.2 Hz, 8H, *p*-C_6H_5), 6.90–6.95 (m, 2H, $C_{18}H_{10}$), 7.01 (t, *J* = 7.2 Hz, 16H, *m*-C_6H_5), 7.07 (t, *J* = 7.2 Hz, 8H, *p*-C_6H_5), 7.15–7.40 (m, 2H, $C_{18}H_{10}$), 7.15–7.40 (m, 2H, $C_{18}H_{10}$), 7.24–7.31 (m, 16H, *o*-C_6H_5), 8.03–8.15 (m, 16H, *o*-C_6H_5), 8.21–8.30 (m, 2H, $C_{18}H_{10}$), 8.94 (s, 2H, $C_{18}H_{10}$). $^{31}P\{^1H\}$ NMR (161 MHz, C_6D_6, r.t.): δ 51.0 (s, dppe). ESI-TOF MS (CH_2Cl_2): *m/z* Calcd. for $C_{140}H_{124}P_8Ru_2Si_2$: 2311.99, Found 2312.53 $[M]^+$. IR (KBr/cm^{-1}): 1935 (m), 1999 (s), 2022 (s), 2113 (s), 2171 (m) ν(C≡C). Anal. Calcd. for $C_{140}H_{124}P_8Ru_2Si_2$ (**5**): C, 73.13; H, 5.14, Found: C, 72.71; H, 5.40.

Synthesis of 6: The title complex **6** was prepared in a manner similar to that of **1** using RuCl(C_4TMS)$(dppe)_2$ (33 mg, 0.032 mmol), $NaBPh_4$ (33 mg, 0.096 mmol), triethylamine (1 mL), 1,2-dichloroethane (10 mL), and a toluene solution of 6,13-diethynylpentacene (20 mL, freshly prepared from 6,13-diethylsilylethynylpentacene (0.032 mmol) following the method B). Before column chromatography, a CH_2Cl_2 solution of cobaltocene (8 mg, 0.042 mmol) was added to the solution to reduce the oxidized species formed during the reaction. The complex **6** was obtained as a green powder (5.4 mg, 0.0023 mmol, 14%). An analytical pure sample and crystals for X-ray analysis were obtained by slow diffusion of hexane into a benzene solution of **6**. ^1H NMR (400 MHz, C_6D_6, r.t.): δ 0.46 (s, 18H, TMS), 2.69–3.00 (m, 16H, dppe-CH_2), 6.59–6.71 (m, 16H, *m*-C_6H_5), 6.59–6.71 (m, 8H, *p*-C_6H_5), 7.00 (t, *J* = 7.2 Hz, 16H, *m*-C_6H_5), 7.07 (t, *J* = 7.2 Hz, 8H, *p*-C_6H_5), 7.12–7.20 (m, 4H, $C_{22}H_{12}$), 7.22–7.30 (m, 16H, *o*-C_6H_5), 7.22–7.30 (m, 4H, $C_{22}H_{12}$), 8.05–8.22 (m, 16H, *o*-C_6H_5), 8.95 (s, 4H, $C_{22}H_{12}$). $^{31}P\{^1H\}$ NMR (161 MHz, C_6D_6, r.t.): δ 51.0 (s, dppe). ESI-TOF MS (CH_2Cl_2): *m/z* Calcd. for $C_{144}H_{126}P_8Ru_2Si_2$: 2362.54, Found 2362.48 $[M]^+$. IR (KBr/cm^{-1}): 1928 (m), 1997 (s), 2014 (s), 2113 (s), 2169 (m) ν(C≡C). Anal. Calcd. for $C_{144.6}H_{127.2}Cl_{1.2}P_8Ru_2Si_2$ (**6**•$(CH_2Cl_2)_{0.6}$): C, 71.96; H, 5.31, Found: C, 71.71; H, 5.29.

Acknowledgements

This work was supported by JSPS KAKENHI Grant Numbers 18 K05139 and 21 K05211. YT acknowledges research grants from ENEOS Tonengeneral Research/Development Encouragement & Scholarship Foundation, The Asahi Glass Foundation, Inamori Foundation, Tokyo Kasei Chemical Promotion foundation and Tokuyama Science Foundation. This work was performed under the Cooperative Research Program of "Network Joint Research Center for Materials and Devices." The computations were performed by using the computer in the Research Center for Computational Science, Okazaki, Japan (21-IMS-C071, 22-IMS-C071). We thank Ms. Keiko Ideta (Kyushu Univ.) and Dr. Atushi Tahara (Tohoku Univ.) for the help of ESR measurements. We acknowledge Dr. Horst Puschmann (Durham Univ.) for his kind help to solve X-ray crystallography.

Conflict of Interest

The authors declare no conflict of interest.

Data Availability Statement

The data that support the findings of this study are available from the corresponding author upon reasonable request.

Keywords: acene · metal acetylide · mixed-valence complex · ruthenium

[1] K. D. Demadis, C. M. Hartshorn, T. J. Meyer, *Chem. Rev.* **2001**, *101*, 2655–2686.
[2] D. M. D'Alessandro, F. R. Keene, *Chem. Soc. Rev.* **2006**, *35*, 424–440.
[3] P. J. Low, *Coord. Chem. Rev.* **2013**, *257*, 1507–1532.
[4] J.-P. Launay, *Coord. Chem. Rev.* **2013**, *257*, 1544–1554.
[5] J.-F. Halet, C. Lapinte, *Coord. Chem. Rev.* **2013**, *257*, 1584–1613.
[6] S. Rigaut, *Dalton Trans.* **2013**, *42*, 15859–15863.
[7] Y.-W. Zhong, Z.-L. Gong, J.-Y. Shao, J. Yao, *Coord. Chem. Rev.* **2016**, *312*, 22–40.
[8] Y. Tanaka, M. Akita, *Coord. Chem. Rev.* **2019**, *388*, 334–342.
[9] S. Gückel, P. Safari, S. M. Bagher Hosseini Ghazvini, M. R. Hall, J. B. G. Gluyas, M. Kaupp, P. J. Low, *Organometallics* **2021**, *40*, 346–357.
[10] S. I. Ghazala, F. Paul, L. Toupet, T. Roisnel, P. Hapiot, C. Lapinte, *J. Am. Chem. Soc.* **2006**, *128*, 2463–2476.

[11] L.-B. Gao, J. Kan, Y. Fan, L.-Y. Zhang, S.-H. Liu, Z.-N. Chen, *Inorg. Chem.* **2007**, *46*, 5651–5664.
[12] J. Zhang, M.-X. Zhang, C.-F. Sun, M. Xu, F. Hartl, J. Yin, G.-A. Yu, L. Rao, S. H. Liu, *Organometallics* **2015**, *34*, 3967–3978.
[13] Y. Tanaka, M. Ono, M. Akita, *J. Porphyrins Phthalocyanines* **2015**, *19*, 442–450.
[14] K. Mishiba, M. Ono, Y. Tanaka, M. Akita, *Chem. Eur. J.* **2016**, *23*, 2067–2076.
[15] Y. Tanaka, M. Ono, M. Akita, *Chem. Lett.* **2018**, *47*, 1296–1299.
[16] N. Le Narvor, C. Lapinte, *Organometallics* **1995**, *14*, 634–639.
[17] F. de Montigny, G. Argouarch, K. Costuas, J.-F. Halet, T. Roisnel, L. Toupet, C. Lapinte, *Organometallics* **2005**, *24*, 4558–4572.
[18] Y. Tanaka, J. A. Shaw-Taberlet, F. Justaud, O. Cador, T. Roisnel, M. Akita, J.-R. Hamon, C. Lapinte, *Organometallics* **2009**, *28*, 4656–4669.
[19] M. A. Fox, B. Le Guennic, R. L. Roberts, D. A. Brue, D. S. Yufit, J. A. K. Howard, G. Manca, J.-F. Halet, F. Hartl, P. J. Low, *J. Am. Chem. Soc.* **2011**, *133*, 18433–18446.
[20] D.-B. Zhang, J.-Y. Wang, H.-M. Wen, Z.-N. Chen, *Organometallics* **2014**, *33*, 4738–4746.
[21] Y.-P. Ou, J. Zhang, M.-X. Zhang, F. Zhang, D. Kuang, F. Hartl, S. H. Liu, *Inorg. Chem.* **2017**, *56*, 11074–11086.
[22] V. I. Minkin, A. G. Starikov, A. A. Starikova, R. M. Minyaev, A. I. Boldyrev, *Dalton Trans.* **2018**, *47*, 15948–15956.
[23] A. A. Starikova, E. A. Metelitsa, V. I. Minkin, *Russ. J. Coord. Chem.* **2019**, *45*, 411–419.
[24] A. A. Starikova, M. G. Chegerev, A. G. Starikov, *Russ. Chem. Bull.* **2020**, *69*, 203–211.
[25] M.-H. Nguyen, J. H. K. Yip, *Organometallics* **2011**, *30*, 6383–6392.
[26] M.-H. Nguyen, J. H. K. Yip, *Organometallics* **2012**, *31*, 7522–7531.
[27] M.-H. Nguyen, V. H. Nguyen, J. H. K. Yip, *Organometallics* **2013**, *32*, 7283–7291.
[28] Y.-P. Ou, J. Zhang, Y. Hu, J. Yin, C. Chi, S. H. Liu, *Dalton Trans.* **2020**, *49*, 16877–16886.
[29] Y. Tanaka, M. Kiguchi, M. Akita, *Chem. Eur. J.* **2017**, *23*, 4741–4749.
[30] K. Sugimoto, Y. Tanaka, S. Fujii, T. Tada, M. Kiguchi, M. Akita, *Chem. Commun.* **2016**, *52*, 5796–5799.
[31] O. A. Al-Owaedi, D. C. Milan, M.-C. Oerthel, S. Bock, D. S. Yufit, J. A. K. Howard, S. J. Higgins, R. J. Nichols, C. J. Lambert, M. R. Bryce, P. J. Low, *Organometallics* **2016**, *35*, 2944–2954.
[32] S. Bock, O. A. Al-Owaedi, S. G. Eaves, D. C. Milan, M. Lemmer, B. W. Skelton, H. M. Osorio, R. J. Nichols, S. J. Higgins, P. Cea, N. J. Long, T. Albrecht, S. Martín, C. J. Lambert, P. J. Low, *Chem. Eur. J.* **2017**, *23*, 2133–2143.
[33] D. C. Milan, A. Vezzoli, I. J. Planje, P. J. Low, *Dalton Trans.* **2018**, *47*, 14125–14138.
[34] Y. Tanaka, Y. Kato, T. Tada, S. Fujii, M. Kiguchi, M. Akita, *J. Am. Chem. Soc.* **2018**, *140*, 10080–10084.
[35] L.-Y. Zhang, P. Duan, J.-Y. Wang, Q.-C. Zhang, Z.-N. Chen, *J. Phys. Chem. C* **2019**, *123*, 5282–5288.
[36] Y. Tanaka, Y. Kato, K. Sugimoto, R. Kawano, T. Tada, S. Fujii, M. Kiguchi, M. Akita, *Chem. Sci.* **2021**, *12*, 4338–4344.
[37] M. Parthey, J. B. G. Gluyas, M. A. Fox, P. J. Low, M. Kaupp, *Chem. Eur. J.* **2014**, *20*, 6895–6908.
[38] K. Sugimoto, H. Idei, Y. Tanaka, M. Akita, *J. Organomet. Chem.* **2017**, *847*, 121–131.
[39] C. Olivier, B. Kim, D. Touchard, S. Rigaut, *Organometallics* **2008**, *27*, 509–518.
[40] Deposition Number(s) 2168516 (for **1**), 2168521 (for **2**), 2168517 (for **3**), 2168520 (for **4**), 2168519 (for **5**), and 2168518 (for **6**) contain(s) the supplementary crystallographic data for this paper. These data are provided free of charge by the joint Cambridge Crystallographic Data Centre and Fachinformationszentrum Karlsruhe Access Structures service.
[41] W. E. Geiger, F. Barrière, *Acc. Chem. Res.* **2010**, *43*, 1030–1039.
[42] A. Heckmann, C. Lambert, *Angew. Chem. Int. Ed.* **2012**, *51*, 326–392; *Angew. Chem.* **2012**, *124*, 334–404.
[43] M. M. Hansmann, M. Melaimi, G. Bertrand, *J. Am. Chem. Soc.* **2018**, *140*, 2206–2213.
[44] M. Parthey, M. Kaupp, *Chem. Soc. Rev.* **2014**, *43*, 5067–5088.
[45] M. Renz, K. Theilacker, C. Lambert, M. Kaupp, *J. Am. Chem. Soc.* **2009**, *131*, 16292–16302.
[46] M. B. Robin, P. Day, *Adv. Inorg. Chem. Radiochem.* **1968**, *10*, 247–422.
[47] J. R. Bolton, *J. Chem. Phys.* **1967**, *46*, 408–409.
[48] S. Schundelmeier, B. Speiser, H. F. Bettinger, R. Einholz, *ChemPhysChem* **2017**, *18*, 2266–2278.
[49] M. Linseis, R. F. Winter, B. Sarkar, W. Kaim, S. Záliš, *Organometallics* **2008**, *27*, 3321–3324.
[50] B. S. Brunschwig, C. Creutz, N. Sutin, *Chem. Soc. Rev.* **2002**, *31*, 168–184.
[51] Y. Tanaka, N. Morozumi, T. Ohto, S. Kaneko, Y. Naitoh, H. Tada, S. Fujii, T. Nishino, M. Akita, **2022**, *ChemRxiv Preprint*, https://doi.org/10.26434/chemrxiv-2022-xfrpb .
[52] M. Akita, Y. Tanaka, *Coord. Chem. Rev.* **2022**, *461*, 214501.

Manuscript received: May 3, 2022
Accepted manuscript online: June 9, 2022
Version of record online: August 4, 2022